International Journal of Nanomedicine

Dovepress
Taylor & Francis Group

Open Access Full Text Article

ORIGINAL RESEARCH

Size-Dependent Layered Double Hydroxide Nanoparticles Promote Osteogenesis and Bone Regeneration via METTL3-Dependent N6-Methyladenosine Modification of Runx2 mRNA

Yang Zhu*, Weiwei Sun*, Yaoyu Huang, Jianxin Li, Haozhe Jiang, Chao Luo, Fuyin Wan, Zhenyu Zhou

Department of Orthopaedics, Affiliated Hospital of Nantong University, Medical School of Nantong University, Nantong, Jiangsu, People's Republic of China

*These authors contributed equally to this work

Correspondence: Fuyin Wan; Zhenyu Zhou, Email jshzwfy@126.com; Tygk858@163.com

Background: The osteogenic efficacy of mesenchymal stem cell (MSC)-based bone regeneration is often limited by insufficient osteogenic differentiation. Layered double hydroxide (LDH) nanoparticles are promising biomaterials, but whether their intrinsic osteoinductive activity is regulated by particle size and epitranscriptomic mechanisms remains unclear. This study investigated whether LDH nanoparticles promote osteogenesis in bone marrow-derived MSCs (BMSCs) through METTL3-dependent N6-methyladenosine (m6A) modification.

Methods: BMSCs were treated with 50 nm or 100 nm LDH nanoparticles under osteogenic induction. Osteogenic differentiation was evaluated by alkaline phosphatase activity, mineralization staining, osteogenic gene/protein expression, and cytoskeletal morphology. Global m6A levels and m6A regulator expression were assessed, and the role of METTL3 was examined using Mettl3 knockdown. Runx2 mRNA m6A enrichment and stability were analyzed by MeRIP-qPCR and actinomycin D chase assays. Bone regeneration was further evaluated using a GelMA-LDH hydrogel in a murine calvarial defect model.

Results: LDH nanoparticles promoted BMSC osteogenesis in a size-dependent manner, with 100 nm LDH producing stronger ALP activity, mineralization, and osteogenic marker expression than 50 nm LDH. Mechanistically, 100 nm LDH increased global m6A methylation and selectively upregulated METTL3. Mettl3 knockdown markedly impaired osteogenesis and abolished the pro-osteogenic effects of LDH. LDH enhanced m6A modification of Runx2 mRNA and prolonged Runx2 transcript stability, thereby supporting RUNX2-mediated osteogenic programming. In vivo, GelMA-LDH implantation significantly enhanced calvarial bone repair and increased RUNX2 and METTL3 expression within defect regions.

Conclusion: Among the two tested particle sizes, 100 nm LDH nanoparticles exhibited superior pro-osteogenic activity and promoted bone regeneration through a METTL3-dependent m6A mechanism that stabilizes Runx2 mRNA.

Keywords: layered double hydroxide, osteogenic differentiation, size-dependent, m6A RNA methylation, METTL3

Introduction

The escalating prevalence of bone defects, including osteoarthritis, osteoporosis, and rheumatoid arthritis, represents a major cause of disability worldwide, particularly in the aging population.[1,2] When innate repair mechanisms are overwhelmed, bone regeneration becomes paramount. Current clinical strategies for bone reconstruction, however, face significant challenges, such as the limited supply and donor-site morbidity of autografts, the risks of infection and immunogenic rejection associated with allografts, and the suboptimal long-term performance of synthetic bone substitutes.[3,4] Although synthetic bone substitutes offer advantages in availability, sterilization, and structural tunability, many clinically used inorganic or polymeric substitutes remain primarily osteoconductive rather than osteoinductive. Their limited ability to actively instruct stem cell osteogenic commitment,

https://doi.org/10.2147/IJN.S611081
Received: 21 March 2026
Accepted: 20 May 2026
Published: 15 June 2026

Graphical Abstract

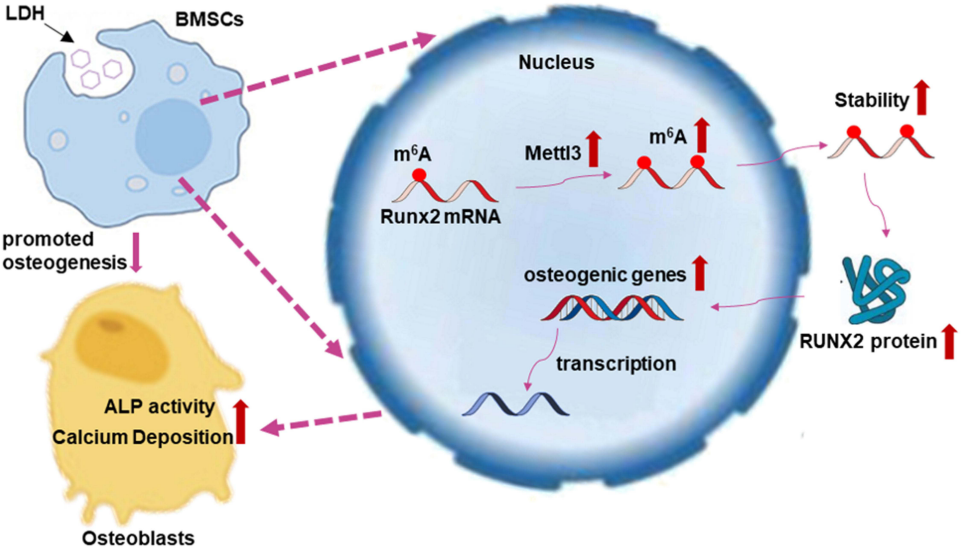

together with mismatched degradation kinetics and incomplete integration with host bone, can compromise long-term regenerative outcomes. Therefore, developing bioactive scaffolds that combine structural support, controlled biodegradability, and intrinsic osteogenic stimulation remains an important challenge in bone tissue engineering.

Bone tissue engineering has leveraged a wide spectrum of biomaterials to direct stem cell fate and differentiation. Many studies have focused on directly activating osteoblasts, the key effector cells in bone formation.[5–7] Among various stem cell sources, mesenchymal stem cells (MSCs) stand out due to their capacities for self-renewal and multi-lineage differentiation,[8,9] making them indispensable for regenerative medicine.

Two-dimensional layered double hydroxides (LDHs) have garnered considerable interest in biomedical applications, including cancer theranostics and drug/gene delivery systems,[10–12] owing to their high specific surface area, excellent biocompatibility and biodegradability, and tunable chemical composition and structure.[13–15] LDHs have also been incorporated into bone cements and implants to enhance their physicochemical and biological properties.[16,17] Despite this, the intrinsic capacity of LDH nanoparticles to induce stem cell differentiation remains poorly understood. A study by Zambuzzi et al demonstrated the osteogenic potential of LDHs in preosteoblasts, enhancing osteogenic marker expression and activating the MAPK signaling pathway.[18] However, preosteoblasts are lineage-committed, whereas MSCs are multipotent. Therefore, investigating the influence of LDHs on MSC fate decision is of greater relevance. Previous reports indicate that LDHs upregulate the expression of key osteogenic markers, including runt-related transcription factor 2 (*Runx2*), osteocalcin (*Ocn*), alkaline phosphatase (*Alp*), osteopontin (*Opn*), and bone morphogenetic protein 2 (*BMP2*) in bone marrow-derived MSCs (BMSCs).[3,17,19] Among these, *Runx2* is a master transcription factor governing MSC commitment to the osteoblastic lineage;[20] its deletion completely blocks osteogenesis at the cartilage stage, underscoring its critical role in early bone formation.[21] *Runx2* directly regulates the expression of downstream bone matrix proteins such as *Opn* and *Ocn*.[22] Nevertheless, the precise molecular mechanism underlying LDH-mediated *Runx2* upregulation in BMSCs is not fully elucidated.

N6-methyladenosine (m6A), the most abundant internal mRNA modification, is dynamically regulated by writers (eg, METTL3, METTL14, WTAP), erasers (FTO, ALKBH5), and readers (YTHDF and IGF2BP proteins).[23,24] This modification plays a crucial role in determining stem cell fate and is intimately involved in skeletal development and homeostasis.[25,26] Notably, Yang et al reported that METTL3 potentiates osteogenesis by augmenting m6A methylation on *Runx2* mRNA, thereby enhancing its stability and expression.[27] However, a potential link between LDH-induced *Runx2* upregulation and m6A modification has not been investigated. Furthermore, unlike previous studies employing single-sized LDH particles, we systematically compared LDH nanoparticles of different sizes (50 nm vs. 100 nm), as nanoparticle size is a critical parameter

influencing cellular uptake and intracellular distribution, which could consequently impact RNA m6A modification processes.[28]

However, most previous studies have focused on the delivery function, ionic bioactivity, or conventional osteogenic signaling pathways of LDH-based materials, whereas whether LDH nanoparticles can regulate osteogenesis through epitranscriptomic remodeling remains unclear. In particular, the relationship among LDH particle size, cellular internalization, METTL3-mediated m6A modification, and Runx2 mRNA stability has not been systematically examined in BMSCs. Therefore, this study aimed to determine whether LDH nanoparticle size modulates BMSC osteogenesis through a METTL3-dependent m6A mechanism.

Materials and Methods

Material Characterization

MgAl-LDH nanoparticles with nominal sizes of 50 nm and 100 nm were commercially sourced from XFNano Co., Ltd. (Nanjing, China) as customized products without public standard catalog numbers. Morphological characterization was performed using transmission electron microscopy (TEM; Hitachi HT7800, Japan). Surface elemental composition was determined by X-ray photoelectron spectroscopy (XPS; Kratos AXIS Supra, UK). Crystalline structure was analyzed via X-ray diffraction (XRD; Bruker D8 Advance, Germany) using Cu Kα radiation. Chemical functional groups were identified by Fourier Transform Infrared spectroscopy (FTIR; PerkinElmer Spectrum Two, USA). Hydrodynamic diameter and zeta potential measurements were conducted using dynamic light scattering (Zetasizer Pro, Malvern Panalytical, UK).

Gelatin methacryloyl (GelMA; Advanced BioMatrix, USA) precursor solution (5% w/v) was homogenized with 200 μL of LDH suspension (2 mg/mL) and photo-crosslinked using UV light for 1 min to fabricate GelMA-LDH nanocomposite hydrogels. The internal microstructure of lyophilized hydrogels was examined by field-emission scanning electron microscopy (FE-SEM; Thermo Scientific Apreo 2, USA).

Cell Culture and Osteogenic Induction

Mouse BMSCs were acquired from American Type Culture Collection (ATCC, USA). Cells were maintained in MEM Alpha Medium (Cytiva, USA) supplemented with 10% fetal bovine serum (FBS; Gibco, USA) and 1% penicillin-streptomycin (Thermo Fisher Scientific, USA) at 37°C in a humidified 5% CO_2 atmosphere. Medium was replenished every 48 h, and cells were subcultured at 80–90% confluence.

For osteogenic differentiation, cells were cultured in osteogenic induction medium consisting of basal medium supplemented with 50 μM ascorbic acid (STEMCELL Technologies, Canada), 10 mM β-glycerophosphate (Alfa Aesar, USA), and 100 nM dexamethasone (Tocris Bioscience, UK). The induction medium was refreshed every two days.

Cytocompatibility Assessment

Cell viability was evaluated using the Cell Counting Kit-8 (CCK-8; MedChemExpress, USA). BMSCs were seeded in 96-well plates (5×10^3 cells/well) and treated with varying concentrations (0–40 μg mL^{-1}) of LDH nanoparticles for 72 h. CCK-8 solution (10 μL/well) was added and incubated for 3 h, followed by absorbance measurement at 450 nm using a microplate reader (BioTek Synergy H1, USA).

Apoptosis was assessed using the Annexin V-APC/7-AAD Apoptosis Detection Kit (BioLegend, USA). BMSCs treated with 40 μg mL^{-1} LDH nanoparticles for 72 h were harvested, stained according to manufacturer's protocol, and analyzed by flow cytometry (Beckman Coulter CytoFLEX, USA).

Cellular Internalization Studies

LDH nanoparticles were fluorescently labeled with FITC (1 mg/mL; Sigma-Aldrich, USA) overnight at 4°C. BMSCs cultured on glass coverslips were treated with FITC-labeled nanoparticles for 24 h, fixed with 4% paraformaldehyde, permeabilized with 0.1% Triton X-100, and stained with Actin-Tracker Red (MedChemExpress, USA) and DAPI (Thermo Fisher Scientific, USA). Cellular uptake was visualized using a confocal laser scanning microscope (Nikon A1R HD25, Japan). For quantitative uptake analysis, BMSCs were incubated with FITC-labeled 50 nm or 100 nm LDH nanoparticles for 24 h. After incubation, cells were

washed thoroughly with PBS to remove extracellular nanoparticles, detached, resuspended in PBS, and analyzed by flow cytometry.

Osteogenic Differentiation Assessment

Alkaline phosphatase (ALP) staining was evaluated after 7 days of osteogenic induction using the BCIP/NBT ALP Development Kit (Vector Laboratories, USA), and ALP activity was quantified using an ALP Activity Assay Kit (Beyotime, Shanghai). Mineralized nodules were stained after 14 days by Alizarin Red S (ARS; ScienCell Research Laboratories, USA), and quantified by dissolving the nodules in 10% cetylpyridinium chloride (CPC, Meilun Biotech). The optical density was measured at 562 nm using a spectrophotometer.

Molecular Analyses

Total RNA was extracted using the RNeasy Mini Kit (Qiagen, Germany). RNA quality was verified by NanoDrop One (Thermo Fisher Scientific, USA). cDNA synthesis was performed using the High-Capacity cDNA Reverse Transcription Kit (Applied Biosystems, USA). Quantitative PCR was conducted on the QuantStudio 5 Real-Time PCR System (Applied Biosystems, USA) using Power SYBR Green Master Mix (Applied Biosystems, USA). Primer sequences are provided in Table S1.

Immunofluorescence Staining

Cells cultured on coverslips were fixed, permeabilized, and blocked with 5% normal donkey serum. The cells were then incubated overnight at 4 °C with primary antibodies against RUNX2 (Santa Cruz Biotechnology, USA) and BMP2 (Santa Cruz Biotechnology, USA). After washing, the cells were incubated with fluorochrome-conjugated secondary antibodies (Jackson ImmunoResearch, USA) for 1 h at room temperature. Nuclei were counterstained with DAPI. Images were captured using a confocal laser scanning microscope.

Dot Blot

Total RNA (500 ng μL^{-1}) was denatured and spotted onto a nylon membrane. The membrane was UV-crosslinked, stained with methylene blue to verify equal RNA loading, and then blocked. Subsequently, the membrane was incubated with an anti-m6A antibody (Synaptic Systems, Germany) overnight at 4 °C, followed by incubation with an HRP-conjugated secondary antibody. The signal was visualized using an enhanced chemiluminescence (ECL) detection system (Tanon, China).

Prediction of Runx2 m6A Methylation Sites

The full-length mRNA sequence of mouse *Runx2* was submitted to the online bioinformatics tool SRAMP to predict high-confidence m6A modification sites (Table S2).

Methylated RNA Immunoprecipitation-qPCR (MeRIP-qPCR)

Total RNA was extracted and fragmented. A portion of the fragmented RNA was saved as the "Input" control. The remaining RNA was subjected to immunoprecipitation using an anti-m6A antibody-coated magnetic beads according to the instructions of the GenSeq m6A MeRIP Kit (Cloudseq, China). The enriched RNA and the input RNA were reverse-transcribed and analyzed by qPCR. The enrichment of m6A-modified Runx2 mRNA was calculated as a percentage of the input.

RNA Stability Assays

BMSCs were treated with 5 $\mu g\ mL^{-1}$ actinomycin D to inhibit transcription. Cells were harvested at 4 h after Act-D treatment. Total RNA was extracted, and the decay of *Runx2* mRNA was analyzed by qRT-PCR.

Genes Knock-Down in BMSCs

The plasmid for the knock-down of *Mettl3* was designed by Generay Biotechnology. BMSCs were transfected with the plasmids using Lipofectamine 3000 (Invitrogen, USA). Stable cell lines were selected with puromycin (2 $\mu g\ mL^{-1}$) for 48 h. Knockdown efficiency was confirmed at both the mRNA and protein levels using qRT-PCR and Western blotting, respectively.

In vivo Evaluation

All animal procedures were approved by the Institutional Animal Care and Use Committee of Affiliated Hospital of Nantong University (Approval No. P20250305-022) and were performed in accordance with the Guide for the Care and Use of Laboratory Animals and the ARRIVE guidelines. Mice were randomly divided into two groups: GelMA and GelMA-LDH, with 3 animals per group. Critical-sized calvarial defects (5 mm in diameter) were created in 8-week-old male C57 mice (Shanghai SLAC Laboratory Animal Co., China) under inhalation anesthesia with isoflurane (3–5% for induction and 1.5–2% for maintenance). Perioperative analgesia was provided with butorphanol (2 mg/kg, subcutaneous injection, every 4 h) as needed after surgery. The defects were then implanted with GelMA or GelMA-LDH composites under aseptic conditions. At 12 weeks after implantation, the animals were euthanized by gradual-fill carbon dioxide inhalation (30–70% chamber volume displacement per minute), followed by cervical dislocation to ensure death, in accordance with applicable veterinary guidelines, including the AVMA Guidelines for the Euthanasia of Animals. The calvarial specimens were then harvested for further analysis.

Histology Analysis

Decalcified specimens were embedded in paraffin and sectioned (6 μm thickness). Sections were stained with Hematoxylin and Eosin (H&E), Masson's Trichrome, and Van Gieson (VG) staining kits (Sigma-Aldrich, USA) following standard protocols. Immunofluorescence staining was performed using antibodies against RUNX2 and METTL3. Systemic biosafety was evaluated by H&E staining of major organs.

Western Blotting

Western blotting was performed to evaluate the protein expression levels of METTL3, RUNX2, and BMP2. Briefly, BMSCs from each treatment group were washed twice with cold PBS and lysed on ice using RIPA lysis buffer supplemented with protease and phosphatase inhibitor cocktails. After centrifugation at 12,000 × g for 15 min at 4 °C, the supernatants were collected, and total protein concentrations were determined using a BCA protein assay kit.

Equal amounts of protein samples were mixed with loading buffer, denatured at 95 °C for 5 min, separated by SDS-PAGE, and transferred onto polyvinylidene fluoride (PVDF) membranes. After transfer, the membranes were blocked with 5% non-fat milk or 5% BSA in TBST for 1 h at room temperature to reduce non-specific binding. The membranes were then incubated overnight at 4 °C with primary antibodies against METTL3 (Santa Cruz Biotechnology, USA), RUNX2 (Santa Cruz Biotechnology, USA), BMP2 (Boster, Wuhan), and GAPDH (Servicebio, Wuhan) at the dilutions recommended by the manufacturers.

After washing three times with TBST, the membranes were incubated with the corresponding horseradish peroxidase (HRP)-conjugated secondary antibodies for 1 h at room temperature. Following another three washes with TBST, protein bands were visualized using an enhanced chemiluminescence (ECL) detection system and imaged with a chemiluminescence imaging system.

Statistical Analysis

Data are presented as mean ± standard deviation. In vitro experiments were performed using three independent biological replicates. For animal experiments, 3 mice were included in each group. Statistical significance was determined by one-way analysis of variance (ANOVA) using GraphPad Prism 10.0 (USA). Significance levels were set at $*p < 0.05$, $**p < 0.01$, and $***p < 0.001$.

Results and Discussion

Structural and Physicochemical Characterization of LDH Nanoparticles

To systematically evaluate the size-dependent bioactivity of LH nanoparticles, two distinct MgAl-LDH samples with diameters of 50 nm and 100 nm were acquired. TEM imaging and DLS analysis confirmed that both LDH exhibited a well-defined hexagonal morphology with uniform size distribution and high monodispersity (Figure 1A and B). XPS survey scans revealed characteristic photoelectron peaks corresponding to Mg 1s, Al 2p, and O 1s core levels, thereby

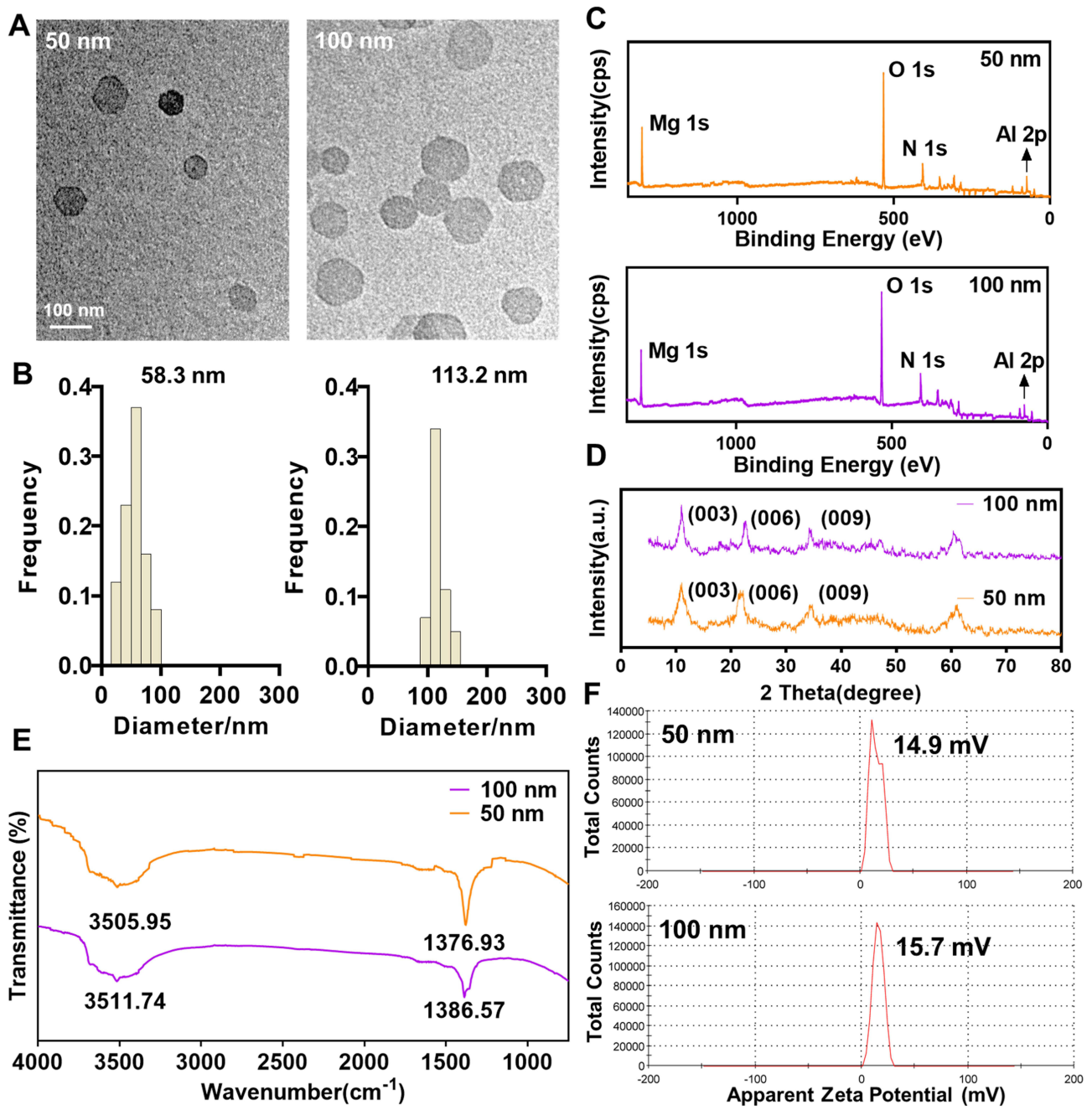

Figure 1 Physicochemical characterization of 50 nm and 100 nm LDH nanoparticles. (**A**) Representative TEM images illustrating the well-defined hexagonal platelet morphology and monodisperse size distribution. (**B**) Hydrodynamic size distribution of nanoparticles determined by DLS. (**C**) XPS survey spectra confirming the presence of constituent elements Mg, Al, O, and N. (**D**) XRD patterns displaying characteristic reflections of the hydrotalcite-like layered structure. (**E**) FTIR spectra identifying characteristic functional groups, including hydroxyl stretches and nitrate vibrations. (**F**) Zeta potential measurements indicating a positively charged surface for both nanoparticles, favorable for cellular interactions.

validating the expected elemental composition (Figure 1C). The crystalline structure was further examined by XRD, which displayed characteristic (003), (006), and (009) reflections indicative of a well-ordered hydrotalcite-like layered structure. Notably, no significant peak shifts or differences in diffraction patterns were observed between the 50 nm and 100 nm LDH, suggesting preserved crystallinity irrespective of particle size (Figure 1D). FTIR spectroscopy identified key vibrational modes, including a broad absorption band around 3500 cm^{-1} attributed to the stretching of structural hydroxyl groups and interlayer water molecules, and a sharp peak near 1380 cm^{-1} corresponding to the stretching vibration of intercalated nitrate anions (Figure 1E). Further analysis of colloidal properties via dynamic light scattering

https://doi.org/10.2147/IJN.S611081

showed that both LDH variants exhibited substantial positive surface charges, with zeta potentials of +14.9 mV and +15.7 mV for the 50 nm and 100 nm particles, respectively (Figure 1F). This pronounced positive surface charge is anticipated to facilitate strong electrostatic interactions with negatively charged cell membrane components, thereby promoting efficient cellular internalization and subsequent intracellular activity. Importantly, these physicochemical features provide a material basis for the subsequent biological responses. Nanoparticle size is a critical determinant of cell–material interactions because it can influence membrane wrapping, endocytic uptake, intracellular trafficking, and retention. In the present study, both 50 nm and 100 nm LDH nanoparticles were within the nanoscale range suitable for cellular internalization; however, their different dimensions may lead to distinct intracellular processing. Together with their positive surface charge, which favors interaction with negatively charged cell membranes, the size difference between the two LDH formulations may contribute to the size-dependent cellular uptake, epitranscriptomic activation, and osteogenic differentiation observed in the following experiments.

Biocompatibility and Cellular Internalization of LDH Nanoparticles

Prior to assessing the osteoinductive potential of the nanoparticles, a comprehensive evaluation of their biocompatibility and cellular uptake behavior was conducted. BMSCs in culture exhibited a characteristic spindle-shaped, fibroblast-like morphology (Figure 2A), and their mesenchymal lineage was confirmed via flow cytometric analysis, which demonstrated positive expression of the canonical surface markers CD29 and CD44, and negligible expression of CD34 and CD45 (Figure 2B).

To quantitatively determine the cytocompatibility of LDH, cell viability was assessed after 72 h of exposure to a concentration gradient (0–40 μg mL^{-1}) using a CCK-8 assay. The results indicated no significant cytotoxicity for either the 50 nm or 100 nm LDH across the entire concentration range tested, confirming their excellent biocompatibility (Figure 2C). This finding was further corroborated by Annexin V-APC/7-AAD apoptosis assays, which revealed high cell viability exceeding 88% in all experimental groups, with no significant increase in early or late apoptotic populations following 40 μg mL^{-1} LDH treatment (Figure 2D). To visualize cellular internalization, LDH nanoparticles were fluorescently labeled with FITC. Confocal laser scanning microscopy after 24 h of incubation clearly showed intracellular green fluorescence in the FITC-LDH treated groups, indicating successful and efficient cellular uptake (Figure 2E). The internalized nanoparticles were predominantly distributed within the cytoplasm, and this process was observable for both LDH. To further quantify nanoparticle internalization, flow cytometry was performed after 24 h of incubation with FITC-labeled LDH nanoparticles. Consistent with the CLSM observations, both 50 nm and 100 nm LDH nanoparticles were efficiently taken up by BMSCs. However, quantitative analysis showed no statistically significant difference between the two LDH groups (Figure S6). These results indicate that although both nanoparticle sizes were readily internalized, the superior osteogenic effect of 100 nm LDH cannot be simply attributed to a higher overall uptake efficiency. This efficient cellular internalization is a critical prerequisite for the subsequent direct intracellular interactions that underpin the observed bioactivity, including the potential modulation of signaling pathways and epitranscriptomic regulatory mechanisms essential for osteogenic lineage commitment.

Size-Dependent Enhancement of Osteogenic Differentiation

We next sought to systematically evaluate the osteoinductive capacity of LDH nanoparticles by examining their influence on the phenotypic and molecular progression of osteogenesis in BMSCs. Consistent with prior reports indicating that BMSCs displayed enlarged cytoskeleton following LDH exposure,[29] our observations confirmed that treatment with both 50 nm and 100 nm LDH prompted significant cellular spreading (Figure 3A and B). These morphological changes are often associated with early osteogenic commitment.

Functional assessment of early osteogenic differentiation, via ALP activity staining after 7 days of induction, revealed a marked enhancement in LDH-treated groups compared to the untreated control (Figure 3C). This was followed by evaluation of late-stage mineralization using ARS staining at day 14, which demonstrated substantially greater calcium nodule deposition in the presence of LDH (Figure 3D). Quantitative analysis showed that 100 nm LDH increased ALP activity by 1.31-fold and mineralized nodule deposition by 1.34-fold compared with 50 nm LDH (Figure 3E and F). Notably, in both functional assays, the 100 nm LDH nanoparticles consistently outperformed their 50 nm counterparts, establishing a clear size-dependent manner in osteogenic potentiation.

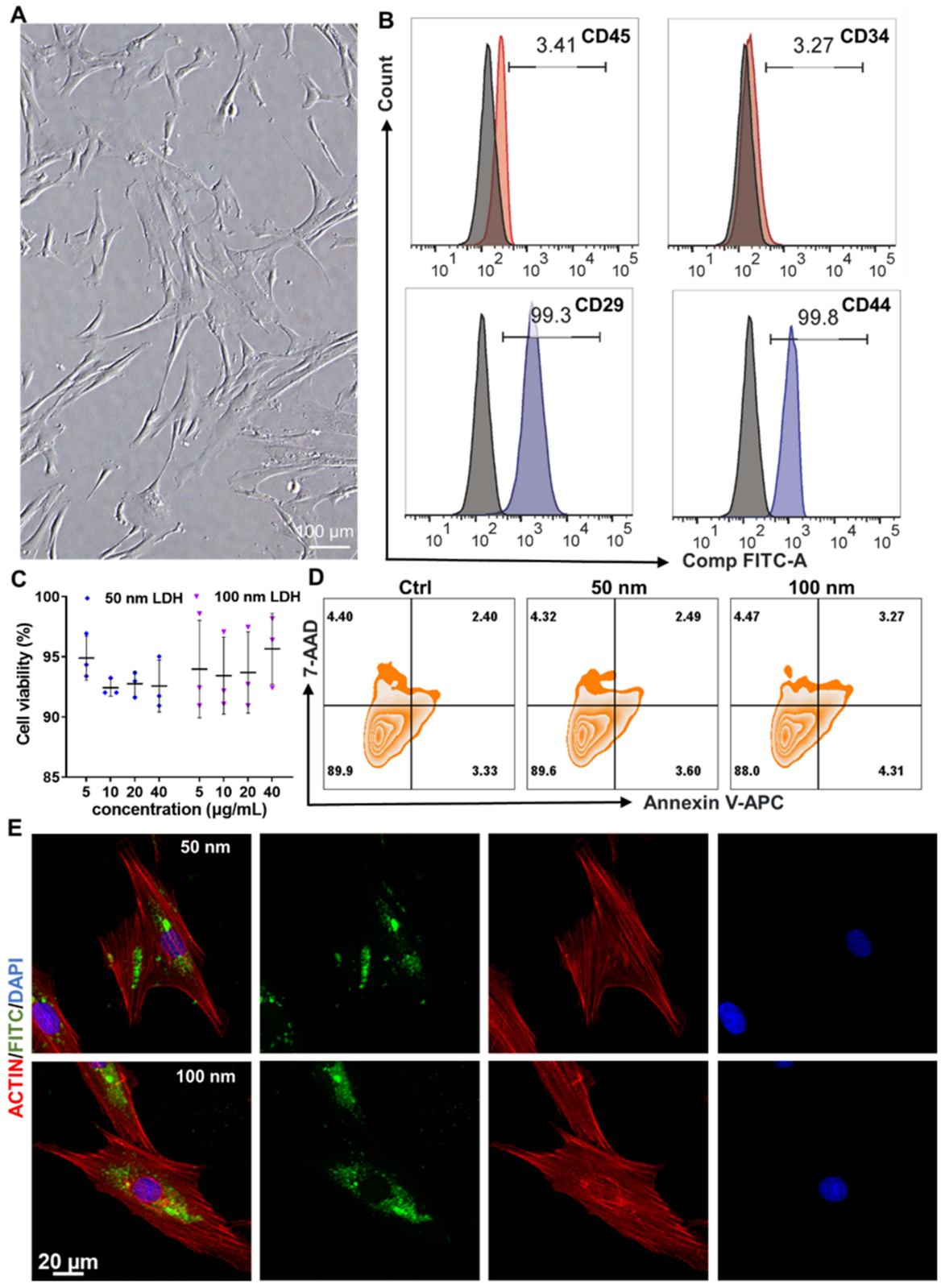

Figure 2 Biocompatibility and cellular internalization of LDH nanoparticles in BMSCs. (**A**) Phase-contrast micrograph showing the characteristic spindle-shaped morphology of BMSCs. (**B**) Flow cytometric analysis validating the mesenchymal stem cell phenotype ($CD29^+/CD44^+/CD34^-/CD45^-$). (**C**) Cell viability assessed by CCK-8 assay after 72 h exposure to increasing concentrations (0–40 μg mL^{-1}) of LDH nanoparticles. (**D**) Quantitative analysis of apoptosis by Annexin V-APC/7-AAD staining, demonstrating high cell viability across all groups. (**E**) Confocal laser scanning microscopy (CLSM) images confirming the efficient intracellular uptake of FITC-labeled LDH nanoparticles (green). F-actin and nuclei are stained with Actin-Tracker Red (red) and DAPI (blue), respectively.

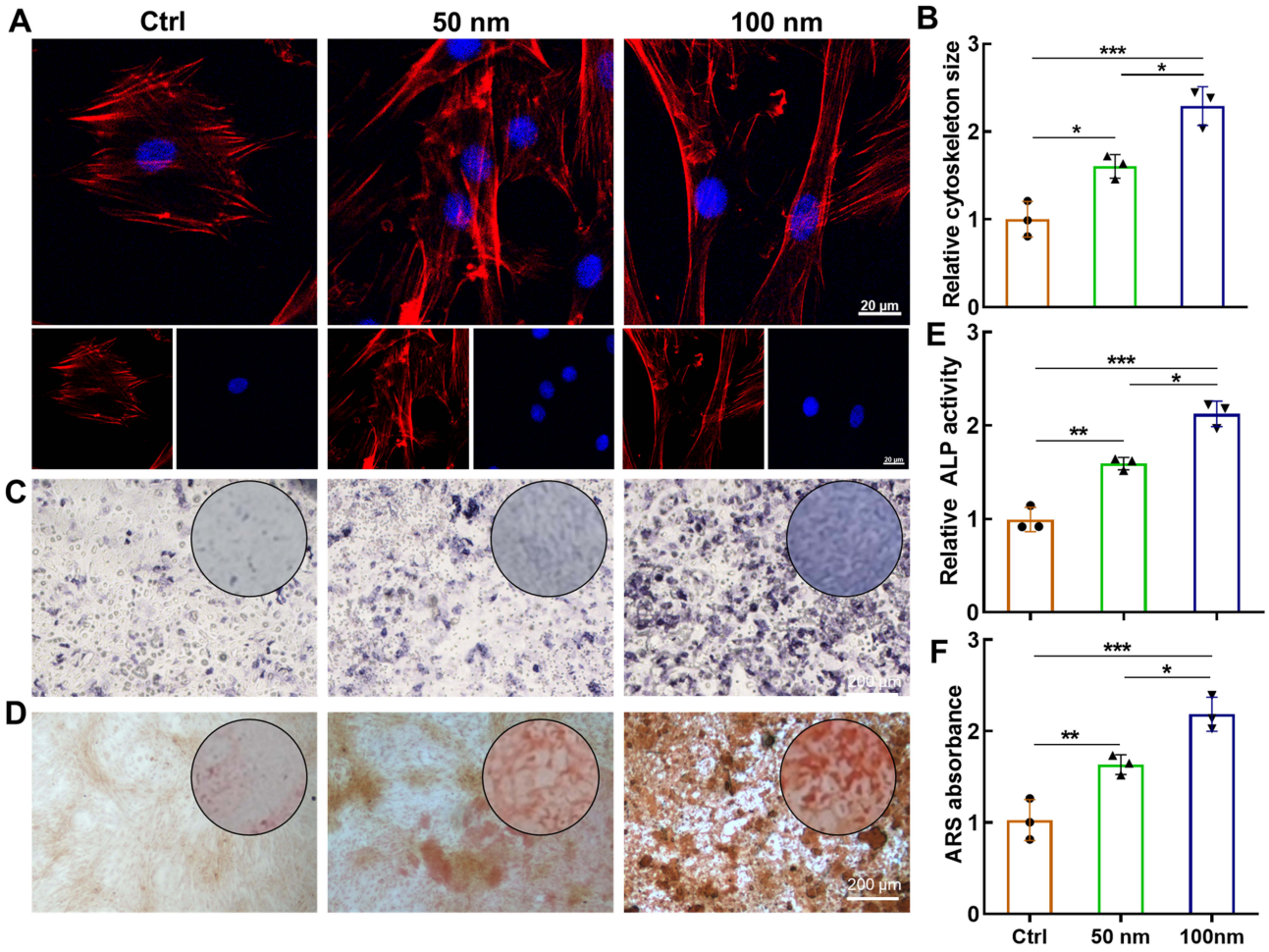

Figure 3 LDH nanoparticles promote osteogenic differentiation of BMSCs in a size-dependent manner. (**A**) Fluorescence images of the cytoskeleton (F-actin, red) and nuclei (DAPI, blue) in BMSCs treated with LDH for 72 h, revealing enhanced cell spreading. (**B**) Quantitative analysis of cell spreading area from (**A**). (**C**) Alkaline phosphatase (ALP) staining after 7 days of osteogenic induction. (**D**) Alizarin Red S (ARS) staining of calcium nodules after 14 days. (**E** and **F**) Quantitative analysis of ALP activity and mineralized nodules, respectively. Data are presented as mean ± SD (n=3). ***p < 0.001, **p < 0.01, *p < 0.05.

To investigate the molecular underpinnings of this enhanced differentiation, we analyzed the expression of key osteogenic genes. Quantitative PCR analysis demonstrated that LDH treatment significantly upregulated the mRNA levels of the master transcription factor *Runx2*, along with its downstream targets, including *Bmp2, Opn*, and *Alp* (Figure 4A). This gene activation was validated by immunofluorescence staining, which showed increased expression of RUNX2 and BMP2 in LDH-treated BMSCs (Figure 4B–E). Western blot analysis further confirmed that LDH treatment increased RUNX2 and BMP2 protein expression, with the strongest upregulation observed in the 100 nm LDH group (Figure S7). The 100 nm LDH group exhibited the most pronounced upregulation, correlating with the superior phenotypic outcomes. Notably, the molecular expression pattern was highly consistent with the functional osteogenic outcomes. The stronger induction of *Runx2, Bmp2, Opn*, and *Alp* mRNA expression, together with increased RUNX2 and BMP2 protein levels, paralleled the enhanced ALP activity and mineralized nodule formation observed in the 100 nm LDH group. These results indicate that LDH-induced molecular osteogenic activation was closely associated with the phenotypic progression of BMSC osteogenic differentiation.

Collectively, these findings substantiate that LDH nanoparticles possess an intrinsic capacity to drive osteogenic differentiation, with efficacy being critically governed by particle size. The 100 nm variant emerged as the most potent inducer, underscoring the importance of nanomaterial dimension in dictating stem cell lineage specification.

https://doi.org/10.2147/IJN.S611081

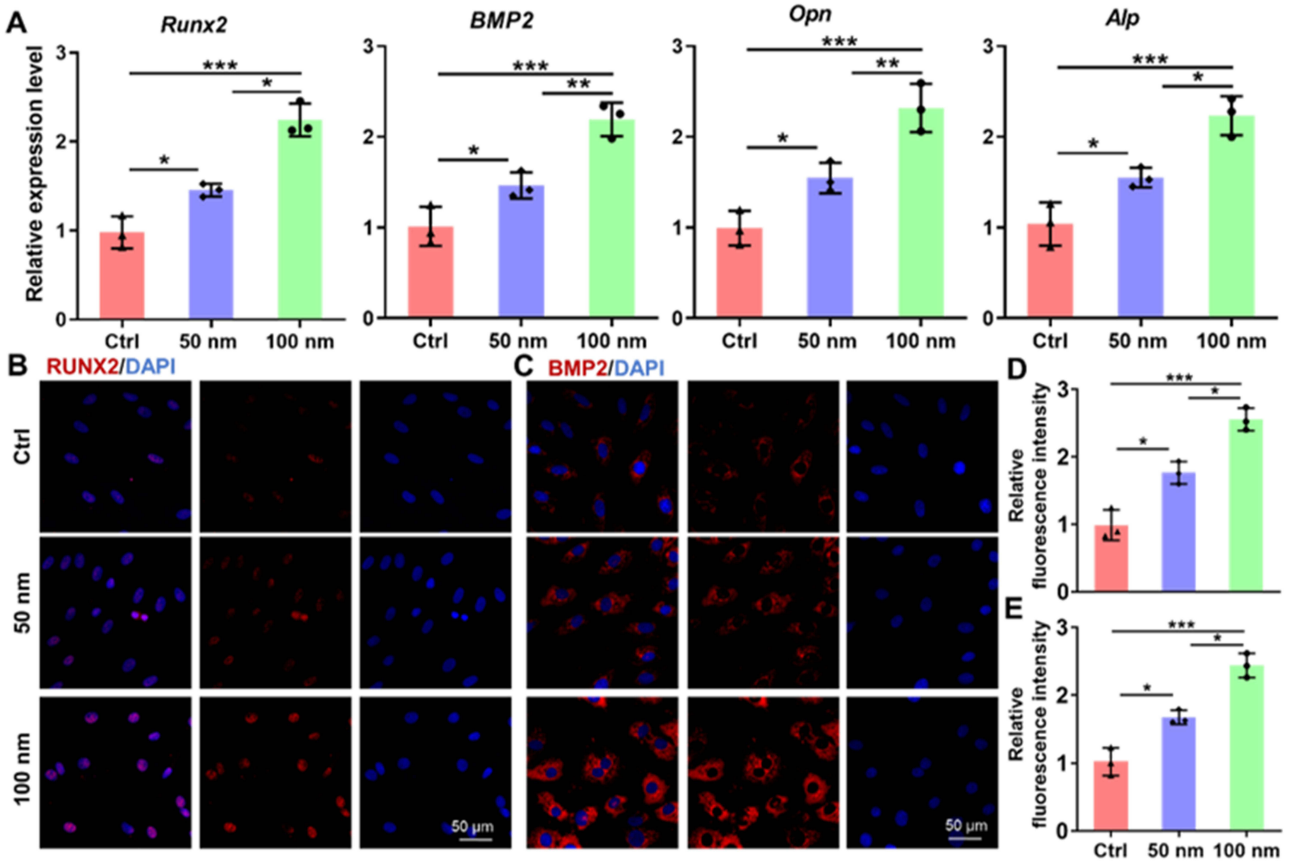

Figure 4 Molecular analysis of osteogenic marker expression upon LDH treatment. (**A**) qRT-PCR analysis of key osteogenic genes (*Runx2, BMP2, Opn* and *Alp*) in BMSCs after 7 days of treatment. (**B** and **C**) Representative immunofluorescence images showing upregulated protein expression of RUNX2 and BMP2 (red) in LDH-treated groups. Nuclei are counterstained with DAPI (blue). (**D** and **E**) Quantitative analysis of the mean fluorescence intensity for RUNX2 and BMP2, respectively. Data are presented as mean ± SD (n=3). ***p < 0.001, **p < 0.01, *p < 0.05.

METTL3-Mediated m6A Methylation in LDH-Induced Osteogenesis

Given the established significance of N6-methyladenosine (m6A) modification in regulating the osteogenic differentiation of BMSCs,[30,31] we sought to investigate whether this epitranscriptomic mechanism contributes to the pro-osteogenic effects of LDH nanoparticles. Dot blot analysis revealed a time-dependent increase in the global m6A methylation level during the course of osteogenic induction (Figure 5A). Notably, treatment with 100 nm LDH resulted in a significant augmentation of the global m6A level on day 7 compared to the untreated control (Figure 5B). To identify the specific regulatory enzymes responsible for this observed increase, we profiled the expression of key m6A "writers" (METTL3, METTL14, WTAP) and "erasers" (FTO, ALKBH5). qPCR analysis demonstrated that the expression of *Mettl3*, which encodes the core catalytic subunit of the m6A methyltransferase complex, was specifically and significantly upregulated upon LDH treatment, whereas the expression of other major regulators remained largely unchanged (Figure 5C). This finding strongly implicated METTL3 as a pivotal mediator in the LDH-driven osteogenesis.

The m6A methyltransferase METTL3 promoted the differentiation of BMSCs into osteoblasts while inhibiting their differentiation into adipocytes.[32,33] Knocking down METTL3 would significantly decreased m6A methylation at numerous sites, which subsequently disrupted the osteogenic differentiation of BMSCs.[34] To functionally validate the necessity of METTL3, we established a stable Mettl3 knockdown (KD) BMSC line. The knockdown efficiency was validated at both the mRNA and protein levels, as confirmed by qRT-PCR and Western blot analysis of METTL3 expression (Figures 5D and S8). METTL3 deficiency led to a profound impairment of the basal osteogenic differentiation capacity, as evidenced by significantly suppressed mRNA expression of key osteogenic markers (*Runx2, Bmp2, Opn, Alp*; Figure 5D), markedly reduced RUNX2 and BMP2 protein levels (Figure 5E and Figure S1–2), and severely compromised ALP activity and matrix

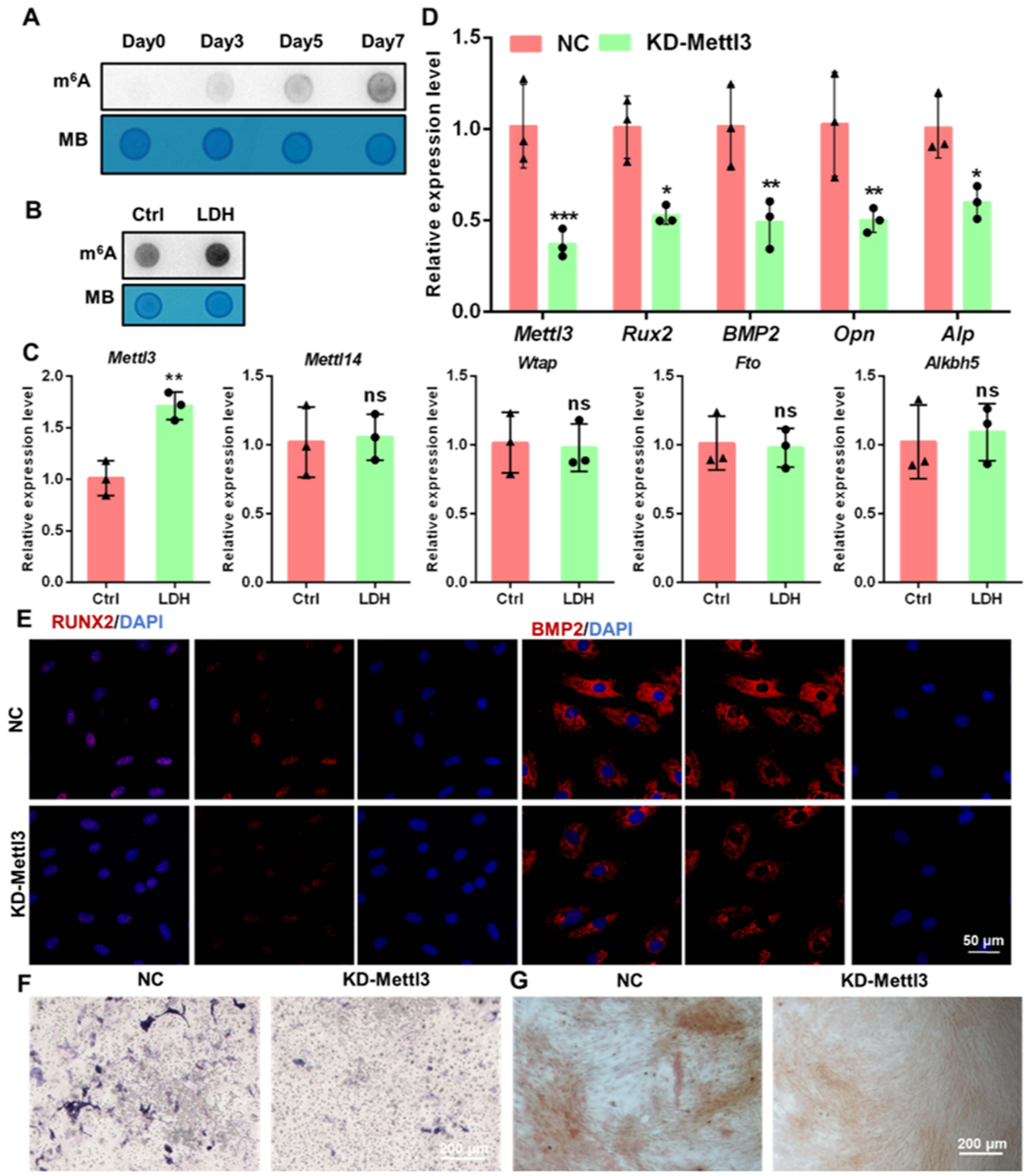

Figure 5 METTL3-mediated m6A methylation is essential for LDH-induced osteogenesis. (**A**) Dot blot analysis showing the temporal increase in global m6A levels during osteogenic differentiation (Days 0–7). (**B**) Enhanced global m6A modification in BMSCs treated with 100 nm LDH on Day 7. (**C**) qRT-PCR analysis of major m6A "writer" (METTL3, METTL14, WTAP) and "eraser" (FTO, ALKBH5) enzymes, highlighting specific Mettl3 upregulation by LDH. (**D**) qRT-PCR analysis of osteogenic genes in NC and Mettl3 knockdown (KD) BMSCs. (**E**) Immunofluorescence analysis of RUNX2 and BMP2 expression in NC and KD cells. (**F** and **G**) ALP and ARS staining, respectively, demonstrating severely impaired osteogenesis upon Mettl3 knockdown. Data are presented as mean ± SD (n=3). ***p < 0.001, **p < 0.01, *p < 0.05.
Abbreviation: ns, not significant.

https://doi.org/10.2147/IJN.S611081

mineralization (Figure 5F and G, Figure S3 and 4). Crucially, the pro-osteogenic effect of LDH was entirely suppressed in Mettl3-KD cells, as LDH treatment failed to promote the expression of osteogenic genes (Figure 6A) or RUNX2 and BMP2 protein levels (Figure 6B and C). Furthermore, the enhanced ALP activity and mineral deposition normally induced by LDH

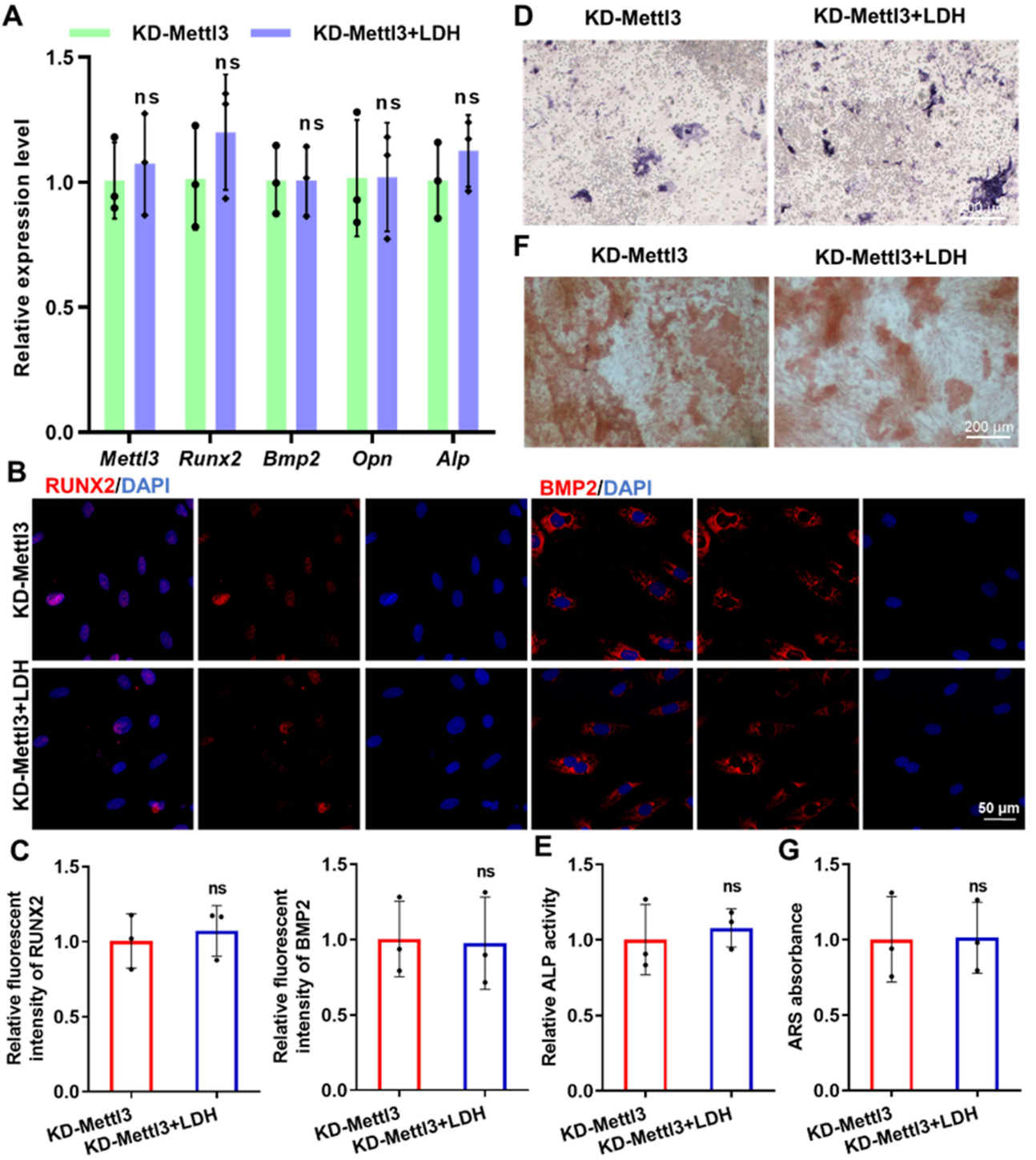

Figure 6 METTL3 deficiency suppresses the pro-osteogenic effect of LDH. (**A**) qRT-PCR analysis of osteogenic gene expression in Mettl3-KD BMSCs with or without 100 nm LHD treatment, showing no rescue effect. (**B** and **C**) Immunofluorescence staining and quantitative analysis confirming that LDH fails to upregulate RUNX2 and BMP2 protein levels in Mettl3-KD cells. (**D**–**G**) ALP and ARS staining, respectively, quantitatively demonstrating that the osteogenic enhancement by LDH is suppressed upon Mettl3 knockdown. Data are presented as mean ± SD (n=3).
Abbreviation: ns, not significant.

were completely suppressed in the Mettl3-KD cells (Figure 6D–G). The inability of LDH to counteract the osteogenic deficit in the Mettl3-KD cells provides compelling genetic evidence that METTL3 is an indispensable effector, through which LDH nanoparticles exert their osteoinductive function.

LDH Enhances m6A Modification and Stability of Runx2 mRNA

Given the central role of *Runx2* as a master transcription factor orchestrating osteogenic lineage commitment,[35] we postulated that its mRNA might be a direct substrate for METTL3-mediated m6A modification in LDH-induced osteogenesis. Bioinformatics analysis using the SRAMP tool identified a high-confidence m6A modification site within the coding sequence of *Runx2* mRNA (Figure 7A and Table S2), suggesting its potential for post-transcriptional regulation via this epitranscriptomic mechanism. To experimentally validate this prediction, MeRIP-qPCR was performed, which demonstrated a significant enrichment of m6A modifications on *Runx2* mRNA in BMSCs treated with 100 nm LDH compared to the untreated control (Figure 7B). Crucially, this LDH-induced hypermethylation was completely suppressed upon Mettl3 knockdown (Figure 7C), providing direct evidence that METTL3 is responsible for the increased m6A deposition on *Runx2* transcripts.

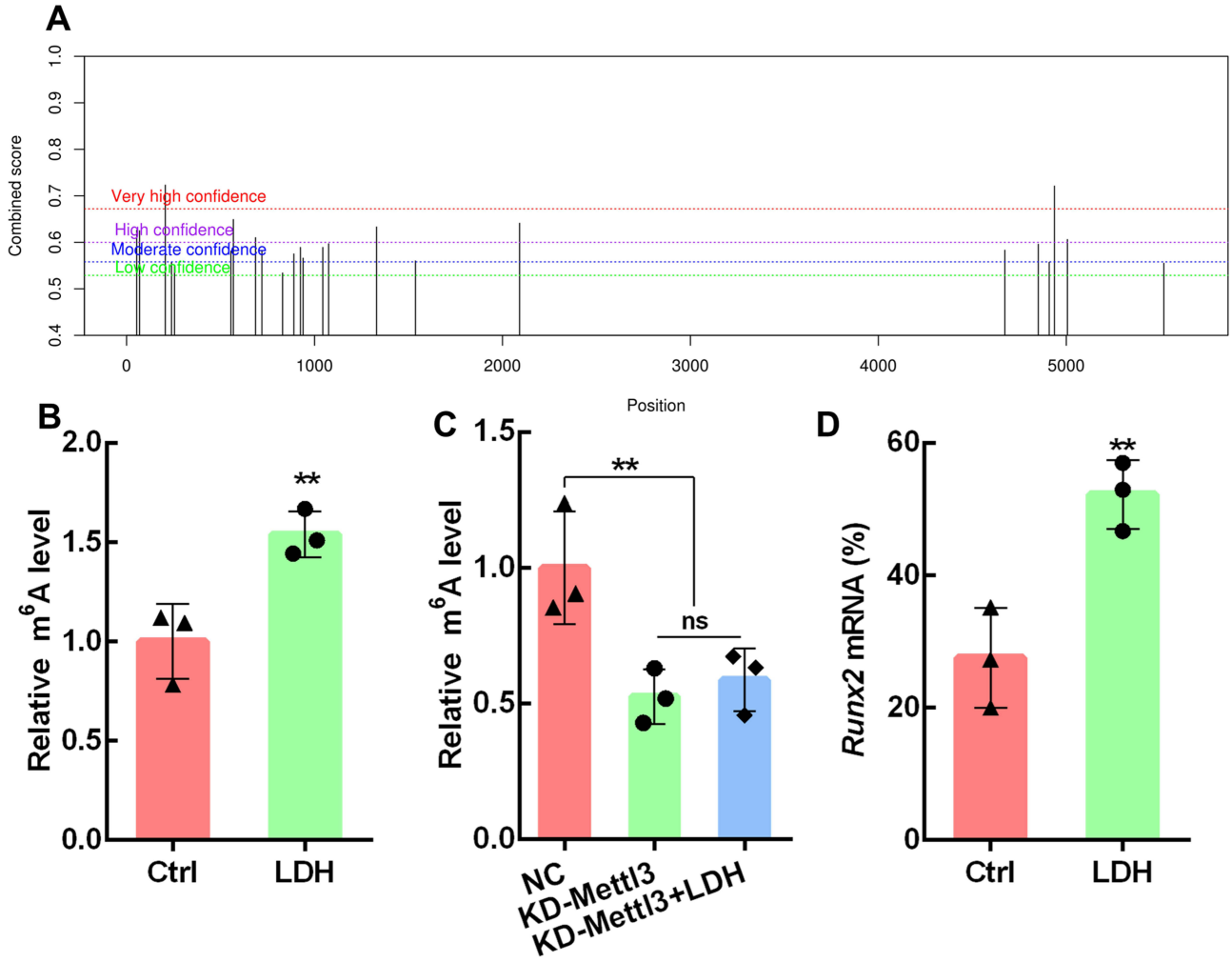

Figure 7 LDH enhances the m6A modification and stability of *Runx2* mRNA. (**A**) Schematic of the predicted high-confidence m6A modification site (red) within the mouse Runx2 mRNA coding sequence (CDS), as identified by the SRAMP bioinformatics tool. (**B**) MeRIP-qPCR analysis showing significant enrichment of m6A on *Runx2* mRNA in BMSCs treated with 100 nm LDH. (**C**) MeRIP-qPCR confirming that Mettl3 knockdown prevents the LDH-induced m6A modification of *Runx2* mRNA. (**D**) *Runx2* mRNA stability assay. BMSCs were treated with Actinomycin D (5 μg mL^{-1}), and the remaining *Runx2* mRNA levels were quantified over time. LDH treatment significantly prolonged the mRNA half-life. Data are presented as mean ± SD (n=3). **p < 0.01.
Abbreviation: ns, not significant.

https://doi.org/10.2147/IJN.S611081

Since m6A modification is known to influence mRNA fate, particularly transcript stability, we next investigated whether this modification affects the half-life of Runx2 mRNA. Actinomycin D chase experiments revealed that treatment with 100 nm LDH significantly decelerated *Runx2* mRNA decay. At 4 h after Act-D treatment, the remaining *Runx2* mRNA level was approximately 52.2% in the LDH-treated group compared with 27.5% in the control group, indicating enhanced Runx2 transcript stability (Figure 7D). This stabilization effect correlates directly with the observed increase in m6A modification, indicating that METTL3-mediated m6A methylation protects *Runx2* transcripts from degradation.

Collectively, these findings reveal that LDH nanoparticles enhance the m6A modification of *Runx2* mRNA in a METTL3-dependent manner. This epitranscriptomic regulation subsequently augments *Runx2* mRNA stability, leading to elevated RUNX2 protein expression and ultimately driving the transcriptional program essential for osteogenic differentiation of BMSCs.

In vivo Bone Regeneration Using GelMA-LDH Nanocomposite Hydrogel

Because 100 nm LDH consistently produced stronger osteogenic responses than 50 nm LDH in ALP activity, mineralization, and osteogenic gene/protein expression, the 100 nm formulation was selected for subsequent in vivo validation. Biomimetic scaffolds provide a robust platform for developing phenotypically stable tissues and facilitating stem cell differentiation.[36] Recent studies demonstrate that hydrogels—natural polymers characterized by high hydration capacity, biocompatibility, and biodegradability—have been integrated with functional additives to potentiate bone regeneration.[19,37,38] GelMA is extensively employed in bone tissue engineering due to its favorable biocompatibility and osteoconductive properties. Notably, Wei et al reported that GelMA hydrogel scaffolds incorporating resveratrol-loaded solid lipid nanoparticles enhance osteogenic differentiation in vitro and bone regeneration in vivo through sustained drug release kinetics.[39] To translate the compelling in vitro findings into a clinically translatable formulation, we engineered a bioactive nanocomposite by incorporating the optimally performing 100 nm LDH nanoparticles into GelMA hydrogel matrix, creating a GelMA-LDH nanocomposite. SEM imaging of the composite revealed a highly porous, three-dimensional microstructure with interconnected pores (Figure 8A), a structure conducive to cell infiltration, nutrient diffusion, and vascularization.

The regenerative efficacy of this nanocomposite was rigorously evaluated in a critical-sized (5 mm diameter) murine calvarial defect model. Micro-CT analysis performed 12 weeks post-implantation demonstrated substantially accelerated bone regeneration in defects treated with the GelMA-LDH composite, compared to those receiving GelMA hydrogel alone (Figures 8B and S9). Quantitative morphometric analysis further showed that GelMA-LDH significantly increased BV/TV, BMD, trabecular number (Tb.N), and trabecular thickness (Tb.Th), while reducing trabecular separation (Tb.Sp), compared with the Blank and GelMA groups (Figure 8C and D, Figure S10).

Histological evaluation through Hematoxylin and Eosin (H&E) and Masson's Trichrome staining provided further evidence of enhanced repair. Defects implanted with the GelMA-LDH composite exhibited extensive deposition of mature, collagen-rich neobone tissue, seamlessly integrating with the native bone edges (Figure 8E). In contrast, GelMA group showed predominantly fibrous tissue infiltration and limited new bone formation.

To confirm that the pro-osteogenic mechanism identified in vitro was operative in vivo, immunofluorescence staining was performed on the harvested bone tissue. Sections from the GelMA-LDH group displayed intense positive staining for both RUNX2 and METTL3 within the defect area (Figure 8F and G), directly linking the observed robust bone regeneration to the upregulation of this key osteogenic transcription factor and its associated epitranscriptomic regulator. Finally, histological examination of major organs (heart, liver, spleen, lungs, and kidneys) and brains from the treated animals showed no evidence of pathological lesions or adverse tissue responses (Figure S5), confirming the systemic biosafety and excellent biocompatibility of the implanted GelMA-LDH nanocomposite.

The pro-osteogenic effect of LDH nanoparticles may not be attributable to a single mechanism. After cellular uptake, LDH nanoparticles may undergo partial intracellular degradation, leading to the gradual release of Mg^{2+} and Al^{3+} ions. Mg^{2+} has been widely implicated in osteogenic differentiation and may contribute to matrix mineralization and osteogenic signaling. However, the present results also suggest that nanoparticle-specific intracellular events are important, because the osteogenic enhancement was closely associated with increased METTL3 expression, elevated m6A modification, and prolonged *Runx2* mRNA stability. In addition, the positively charged LDH surface may facilitate interactions with negatively charged cell membranes and promote endocytic uptake, which could trigger downstream signaling cascades before or during intracellular ion release. Therefore, we

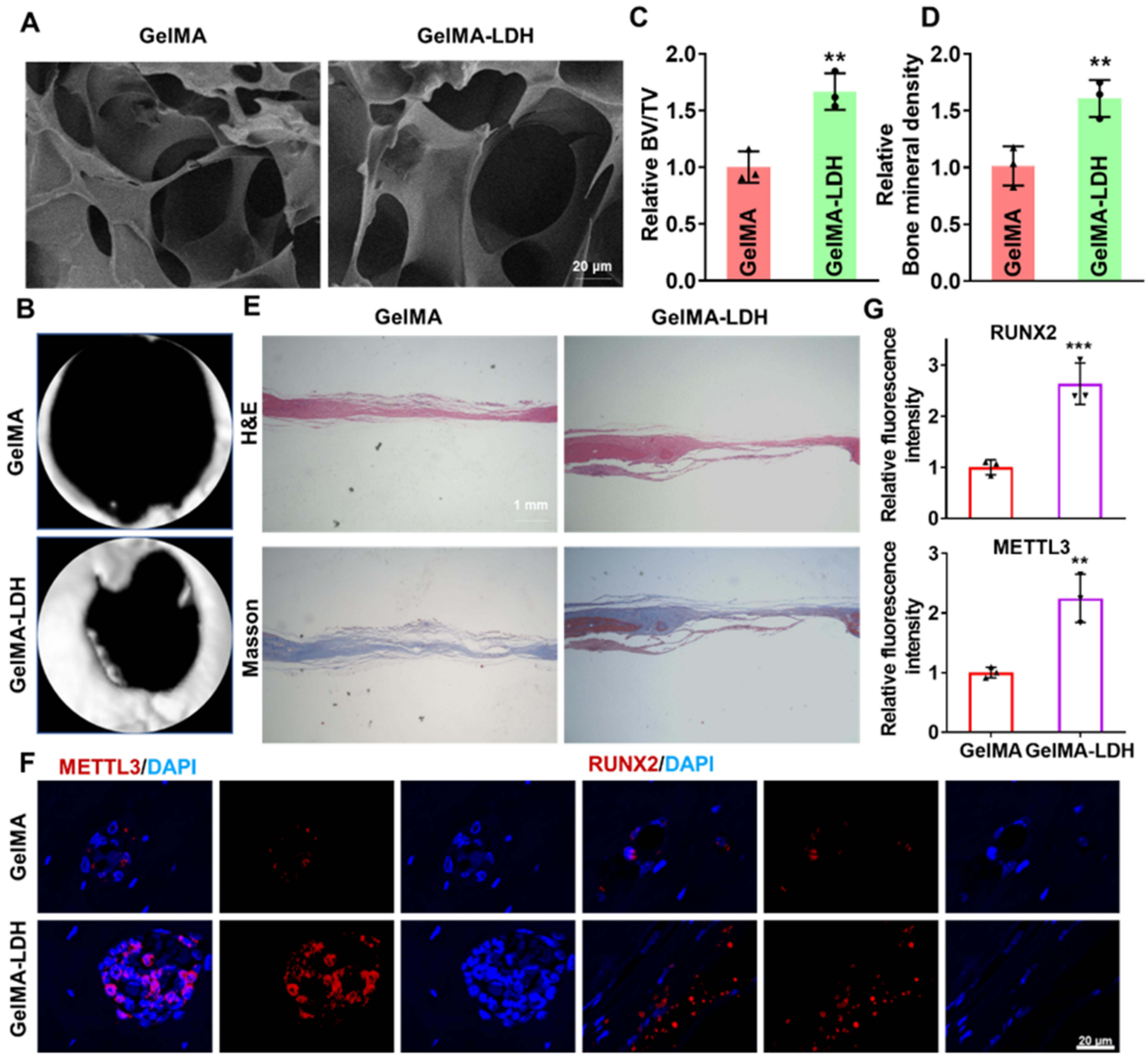

Figure 8 In vivo bone regeneration using a GelMA-LDH composite hydrogel. (**A**) FE-SEM images revealing the highly porous, interconnected microstructure of pure GelMA and GelMA-LDH hydrogels. (**B**) Representative 3D reconstructed micro-CT images of calvarial defects 12 weeks post-implantation in GelMA and GelMA-LDH groups. (**C** and **D**) Quantitative morphometric analysis of bone volume/tissue volume (BV/TV) and bone mineral density (BMD) from micro-CT data. (**E**) Histological evaluation by H&E and Masson's Trichrome staining. (**F** and **G**) Immunofluorescence staining and quantitative analysis of RUNX2 and METTL3 in bone tissue sections from the defect areas. Data are presented as mean ± SD. ***$p < 0.001$, **$p < 0.01$.

speculate that LDH-induced osteogenesis involves the combined effects of membrane interaction, endocytosis-dependent intracellular processing, and ion-mediated bioactivity rather than simple ion supplementation alone.

The stronger METTL3 induction observed with 100 nm LDH may be related to size-dependent differences in cellular uptake and intracellular fate. Nanoparticle size can influence membrane wrapping, endocytic route selection, lysosomal trafficking, and intracellular degradation kinetics. Compared with smaller nanoparticles, 100 nm LDH may achieve a more favorable balance between efficient cellular internalization and sustained intracellular retention, thereby producing a more persistent intracellular stimulus for METTL3 upregulation and m6A remodeling. Nevertheless, the precise upstream signaling events linking LDH internalization to METTL3 activation remain to be further elucidated.

Although our data identify *Runx2* mRNA as a functionally relevant METTL3-dependent target, m6A-mediated regulation usually requires coordinated actions of reader proteins, such as YTHDF and IGF2BP family members. These readers may

https://doi.org/10.2147/IJN.S611081

determine whether m6A-marked transcripts undergo stabilization, translation, or degradation. Therefore, additional m6A reader proteins and downstream osteogenic transcripts may also contribute to the LDH-induced phenotype. Future transcriptome-wide m6A sequencing and reader-specific loss-of-function studies will be required to define the broader epitranscriptomic network regulated by LDH nanoparticles.

Several translational barriers should also be considered. First, the long-term degradation behavior and local ion-release kinetics of GelMA-LDH composites need to be systematically characterized in large-animal bone defect models. Second, although no obvious systemic toxicity was observed in this study, chronic biosafety, immunological responses, and potential accumulation of inorganic components require further evaluation. Third, scalable manufacturing, batch-to-batch reproducibility, sterilization compatibility, storage stability, and regulatory requirements for nanoparticle-containing hydrogel implants must be addressed before clinical translation. Finally, load-bearing bone defects may require further optimization of the mechanical properties of the GelMA-LDH hydrogel.

Conclusion

In summary, this study provides the first evidence linking LDH nanoparticle-induced osteogenic differentiation to m6A RNA methylation. We identified a pronounced size-dependent effect, with 100 nm LDH exhibiting superior efficacy in promoting osteogenesis of BMSCs. Our mechanistic investigation revealed that LDH upregulates the expression of the methyltransferase METTL3, leading to enhanced m6A modification of *Runx2* mRNA. This epitranscriptomic regulation increases the stability of *Runx2* transcripts, resulting in elevated RUNX2 protein levels, which in turn drives the expression of downstream osteogenic genes and facilitates bone regeneration in vivo. These findings not only elucidate a novel molecular pathway underlying the bioactivity of LDH nanomaterials but also provide a foundational framework for designing advanced biomaterials that harness epigenetic and epitranscriptomic mechanisms to precisely control stem cell fate for regenerative medicine.

Acknowledgments

This study was supported by the Young Scientists Fund of the National Natural Science Foundation of China (Grant No. 82502183) and the Scientific Research Project of Nantong Municipal Health Commission (QNZ2024009).

Author Contributions

All authors made a significant contribution to the work reported, whether that is in the conception, study design, execution, acquisition of data, analysis and interpretation, or in all these areas; took part in drafting, revising or critically reviewing the article; gave final approval of the version to be published; have agreed on the journal to which the article has been submitted; and agree to be accountable for all aspects of the work.

Disclosure

The authors report no conflicts of interest in this work.

References

1. Zhou B, Jiang X, Zhou X, et al. GelMA-based bioactive hydrogel scaffolds with multiple bone defect repair functions: therapeutic strategies and recent advances. *Biomater Res*. 2023;27(1):86. doi:10.1186/s40824-023-00422-6
2. LaGuardia JS, Shariati K, Bedar M, et al. Convergence of calcium channel regulation and mechanotransduction in skeletal regenerative biomaterial design. *Adv Healthc Mater*. 2023;12(27):e2301081. doi:10.1002/adhm.202301081
3. Yang L, He X, Jing G, et al. Layered double hydroxide nanoparticles with osteogenic effects as miRNA carriers to synergistically promote osteogenesis of MSCs. *ACS Appl Mater Interfaces*. 2021;13(41):48386–48402. doi:10.1021/acsami.1c14382
4. Bai Y, Wang Z, He X, et al. Application of bioactive materials for osteogenic function in bone tissue engineering. *Small Meth*. 2024;21:e2301283. doi:10.1002/smtd.202301283
5. Tonellato M, Piccione M, Gasparotto M, et al. Commitment of autologous human multipotent stem cells on biomimetic Poly-L-lactic acid-based scaffolds is strongly influenced by structure and concentration of carbon nanomaterial. *Nanomaterials*. 2020;10(3):415. doi:10.3390/nano10030415
6. He Y, Jiang H, Dong S. Bioactives and biomaterial construction for modulating osteoclast activities. *Adv Healthc Mater*. 2024;13(6):e2302807. doi:10.1002/adhm.202302807
7. Barik D, Shyamal S, Das K, et al. Glycoprotein injectable hydrogels promote accelerated bone regeneration through angiogenesis and innervation. *Adv Healthc Mater*. 2023;12(32):e2301959. doi:10.1002/adhm.202301959
8. Lagneau N, Tournier P, Nativel F, et al. Harnessing cell-material interactions to control stem cell secretion for osteoarthritis treatment. *Biomaterials*. 2023;296:122091. doi:10.1016/j.biomaterials.2023.122091

9. Bakadia BM, Qaed Ahmed AA, Lamboni L, et al. Engineering homologous platelet-rich plasma, platelet-rich plasma-derived exosomes, and mesenchymal stem cell-derived exosomes-based dual-crosslinked hydrogels as bioactive diabetic wound dressings. *Bioact Mater*. 2023;28:74–94. doi:10.1016/j.bioactmat.2023.05.002
10. Prasher P, Sharma M. Layered double hydroxide nanocarriers: potential delivery systems for mefenamic acid. *Nanomedicine*. 2023;18 (24):1697–1701. doi:10.2217/nnm-2023-0217
11. Kim TH, Young Lee J, Xie J, et al. Topology dependent modification of layered double hydroxide for therapeutic and diagnostic platform. *Adv Drug Deliv Rev*. 2022;188:114459. doi:10.1016/j.addr.2022.114459
12. Lee J, Seo HS, Park W, et al. Biofunctional layered double hydroxide nanohybrids for cancer therapy. *Materials*. 2022;15(22):7977. doi:10.3390/ma15227977
13. Chang M, Wang M, Liu B, et al. A cancer nanovaccine based on an FeAl-layered double hydroxide framework for reactive oxygen species-augmented metalloimmunotherapy. *ACS Nano*. 2024;18(11):8143–8156. doi:10.1021/acsnano.3c11960
14. Wang Z, Bai Y, Xu X, et al. Two-way regulation of MgFe-LDH on ESC cell fate via temporal selective activation of different cell membrane receptors. *Adv Funct Mater*. 2024;34:2314112. doi:10.1002/adfm.202314112
15. Zhao Y, Zhang P, Liang J, et al. Unlocking layered double hydroxide as a high-performance cathode material for aqueous zinc-ion batteries. *Adv Mater*. 2022;34(37):e2204320. doi:10.1002/adma.202204320
16. Cheng S, Zhang D, Li M, et al. Osteogenesis, angiogenesis and immune response of Mg-Al layered double hydroxide coating on pure Mg. *Bioact Mater*. 2021;6(1):91–105. doi:10.1016/j.bioactmat.2020.07.014
17. Wang Y, Shen S, Hu T, et al. Layered double hydroxide modified bone cement promoting osseointegration via multiple osteogenic signal pathways. *ACS Nano*. 2021;15(6):9732–9745. doi:10.1021/acsnano.1c00461
18. Kang HR, da Costa Fernandes CJ, da Silva RA, et al. Mg–Al and Zn–Al layered double hydroxides promote dynamic expression of marker genes in osteogenic differentiation by modulating mitogen-activated protein kinases. *Adv Healthcare Mater*. 2018;7(4):1700693. doi:10.1002/adhm.201700693
19. Lv Z, Hu T, Bian Y, et al. A MgFe-LDH nanosheet-incorporated smart thermo-responsive hydrogel with controllable growth factor releasing capability for bone regeneration. *Adv Mater*. 2023;35(5):e2206545. doi:10.1002/adma.202206545
20. Takahata Y, Hagino H, Kimura A, et al. Smoc1 and Smoc2 regulate bone formation as downstream molecules of Runx2. *Commun Biol*. 2021;4 (1):1199. doi:10.1038/s42003-021-02717-7
21. Hesse E, Saito H, Kiviranta R, et al. Zfp521 controls bone mass by HDAC3-dependent attenuation of Runx2 activity. *J Cell Biol*. 2010;191 (7):1271–1283. doi:10.1083/jcb.201009107
22. Liu JC, Lengner CJ, Gaur T, et al. Runx2 protein expression utilizes the Runx2 P1 promoter to establish osteoprogenitor cell number for normal bone formation. *J Biol Chem*. 2011;286(34):30057–30070. doi:10.1074/jbc.M111.241505
23. Sendinc E, Shi Y. RNA m6A methylation across the transcriptome. *Mol Cell*. 2023;83(3):428–441. doi:10.1016/j.molcel.2023.01.006
24. Zhuang H, Yu B, Tao D, et al. The role of m6A methylation in therapy resistance in cancer. *Mol Cancer*. 2023;22(1):91. doi:10.1186/s12943-023-01782-2
25. Gu Y, Song Y, Pan Y, et al. The essential roles of m(6)A modification in osteogenesis and common bone diseases. *Genes Dis*. 2024;11(1):335–345. doi:10.1016/j.gendis.2023.01.032
26. Zou Z, He T, Liu Y, et al. Emerging role of m6A modification in osteogenesis of stem cells. *J Bone Miner Metab*. 2022;40(2):177–188. doi:10.1007/s00774-021-01297-0
27. Yan G, Yuan Y, He M, et al. m(6)A methylation of precursor-miR-320/RUNX2 controls osteogenic potential of bone marrow-derived mesenchymal stem cells. *Mol Ther Nucleic Acids*. 2020;19:421–436. doi:10.1016/j.omtn.2019.12.001
28. Bai Y, Zhu Y, He X, et al. Size-optimized layered double hydroxide nanoparticles promote neural progenitor cells differentiation of embryonic stem cells through the regulation of M(6)A methylation. *Int J Nanomed*. 2024;19:4181–4197. doi:10.2147/IJN.S463141
29. Wang Z, Yang H, Xu X, et al. Ion elemental-optimized layered double hydroxide nanoparticles promote chondrogenic differentiation and intervertebral disc regeneration of mesenchymal stem cells through focal adhesion signaling pathway. *Bioact Mater*. 2022;22:75–90. doi:10.1016/j.bioactmat.2022.08.023
30. You Y, Liu J, Zhang L, et al. WTAP-mediated m(6)A modification modulates bone marrow mesenchymal stem cells differentiation potential and osteoporosis. *Cell Death Dis*. 2023;14(1):33. doi:10.1038/s41419-023-05565-x
31. Zhang Q, Li J, Wang C, et al. N6-methyladenosine in cell-fate determination of BMSCs: from mechanism to applications. *Research*. 2024;7 (7):0340. doi:10.34133/research.0340
32. Zhou S, Zhang G, Wang K, et al. METTL3 potentiates osteogenic differentiation of bone marrow mesenchymal stem cells via IGF2BP1 / m6A / RUNX2. *Oral Dis*. 2024;30(3):1313–1321. doi:10.1111/odi.14526
33. Xie Z, Luo H, Wang T, et al. METTL3 inhibits BMSC apoptosis and facilitates osteonecrosis repair via an m6A-IGF2BP2-dependent mechanism. *Heliyon*. 2024;10(10):e30195. doi:10.1016/j.heliyon.2024.e30195
34. Zhang Y, Kong Y, Zhang W, et al. METTL3 promotes osteoblast ribosome biogenesis and alleviates periodontitis. *Clin Clin Epigenet*. 2024;16 (1):18. doi:10.1186/s13148-024-01628-8
35. Kim P, Park J, Lee DJ, et al. Mast4 determines the cell fate of MSCs for bone and cartilage development. *Nat Commun*. 2022;13(1):3960. doi:10.1038/s41467-022-31697-3
36. Kim HD, Amirthalingam S, Kim SL, et al. Biomimetic materials and fabrication approaches for bone tissue engineering. *Adv Healthc Mater*. 2017;6(23). doi:10.1002/adhm.201700612.
37. Wu J, Zheng K, Huang X, et al. Thermally triggered injectable chitosan/silk fibroin/bioactive glass nanoparticle hydrogels for in-situ bone formation in rat calvarial bone defects. *Acta Biomater*. 2019;91:60–71. doi:10.1016/j.actbio.2019.04.023
38. Kurian AG, Singh RK, Patel KD, et al. Multifunctional GelMA platforms with nanomaterials for advanced tissue therapeutics. *Bioact Mater*. 2022;8:267–295. doi:10.1016/j.bioactmat.2021.06.027
39. Wei B, Wang W, Liu X, et al. Gelatin methacrylate hydrogel scaffold carrying resveratrol-loaded solid lipid nanoparticles for enhancement of osteogenic differentiation of BMSCs and effective bone regeneration. *Regen Biomater*. 2021;8(5):rbab044. doi:10.1093/rb/rbab044